Petroleum Science 21 (2024) 1660–1670

Contents lists available at ScienceDirect

Petroleum Science

journal homepage: www.keaipublishing.com/en/journals/petroleum-science

Original Paper

Full waveform inversion based on hybrid gradient

Chuang Xie [a, b], Zhi-Liang Qin [a, b, *], Jian-Hua Wang [c], Peng Song [d], Heng-Guang Shen [e], Sheng-Qi Yu [a, b], Ben-Jun Ma [a, b], Xue-Qin Liu [a, b]

[a] Qingdao Innovation and Development Base, Harbin Engineering University, Qingdao, 266000, Shandong, China
[b] Qingdao Innovation and Development Center, Harbin Engineering University, Qingdao, 266000, Shandong, China
[c] CNOOC Research Institute Co., Ltd., Beijing, 100028, China
[d] College of Marine Geoscience, Ocean University of China, Qingdao, 266100, Shandong, China
[e] Weihai Sunfull Geophysical Exploration Equipment Co., Ltd., Weihai, 264209, Shandong, China

ARTICLE INFO

Article history:
Received 13 April 2023
Received in revised form
4 November 2023
Accepted 15 January 2024
Available online 20 January 2024

Edited by Jie Hao and Meng-Jiao Zhou

Keywords:
Full waveform inversion
Hybrid gradient
Scattering angle weighted
Low-wavenumber component

ABSTRACT

The low-wavenumber components in the gradient of full waveform inversion (FWI) play a vital role in the stability of the inversion. However, when FWI is implemented in some high frequencies and current models are not far away from the real velocity model, an excessive number of low-wavenumber components in the gradient will also reduce the convergence rate and inversion accuracy. To solve this problem, this paper firstly derives a formula of scattering angle weighted gradient in FWI, then proposes a hybrid gradient. The hybrid gradient combines the conventional gradient of FWI with the scattering angle weighted gradient in each inversion frequency band based on an empirical formula derived herein. Using weighted hybrid mode, we can retain some low-wavenumber components in the initial low-frequency inversion to ensure the stability of the inversion, and use more high-wavenumber components in the high-frequency inversion to improve the convergence rate. The results of synthetic data experiment demonstrate that compared to the conventional FWI, the FWI based on the proposed hybrid gradient can effectively reduce the low-wavenumber components in the gradient under the premise of ensuring inversion stability. It also greatly enhances the convergence rate and inversion accuracy, especially in the deep part of the model. And the field marine seismic data experiment also illustrates that the FWI based on hybrid gradient (HGFWI) has good stability and adaptability.

1. Introduction

The FWI method was proposed by Tarantola (1984) in the early 1980s. In this method, all waveform information in the simulated and observed data was used to construct the L2-norm objective function, and the gradient was calculated by adopting the adjoint state method. Using an optimization algorithm, the given initial velocity model was continuously updated iteratively according to the gradient, and the high-resolution inversion result of the subsurface structures was obtained. Due to the potential of FWI to describe the velocity model of complex underground structures, this method has been widely discussed, and has become a research hotspot in the field of geophysics (Chen et al., 2018; Jakobsen and Wu, 2018; Ren et al., 2019, 2023; Song et al., 2019; Yao et al., 2019b; Fu et al., 2020; Yang et al., 2020; Li and Alkhalifah, 2021; Li et al., 2022; Ke et al., 2023).

The gradient of FWI is usually calculated by applying cross-correlation between the forward-propagated wavefield of sources and the back-propagated wavefield of residual records. The wavenumber component of the gradient is related to the frequency component of the data and the scattering angle between the shot and receiver points (Alkhalifah, 2015). Thus, when FWI is implemented in some low-frequency bands, numerous low-wavenumber components that help avoid the cycle skipping of low-frequency inversion are available. In recent years, many experts and scholars have studied the application of low-wavenumber components in the gradient to reduce the dependence of FWI on initial velocity models. Shipp and Singh (2002) applied large offset data to large-scale structures because large offset data generally correspond to large scattering angle information. Tang et al. (2013) used scattering angle information to separate the low-wavenumber and

* Corresponding author.
E-mail address: qin_zhiliang@126.com (Z.-L. Qin).

https://doi.org/10.1016/j.petsci.2024.01.013

high-wavenumber components in the gradient of FWI and increased the weight of the low-wavenumber components to improve the inversion ability of large-scale structures. Alkhalifah (2015) directly performed scattering angle filtering on the gradient of FWI, and applied the large scattering angle (low-wavenumber) information close to 180° to construct a highly accurate initial model. Based on this, Alkhalifah and Wu (2016) combined such information with multiple scattering information to enrich the effective low-wavenumber components. Yao et al. (2018) achieved the separation of tomography and migration components in the plane wave domain and verified the effectiveness and stability of the method in field seismic data processing. Huang et al. (2018) developed a hybrid multi-scale FWI method based on a frequency-wavenumber filter, which improved the robustness of the multi-scale inversion method. Lian et al. (2018) adopted tomography components from the gradient for inversion and obtained satisfactory experimental results in noisy and low-frequency missing seismic data. Yao et al. (2019a) transformed the gradient into the wavenumber domain for filtering and extracted the tomographic components using nonstationary smoothing. Li et al. (2022) proposed a multi-scale FWI method based on gradient decomposition in the wavenumber domain, which obtained a high-precision initial model.

However, when FWI is implemented in some high-frequency bands, a large number of low-wavenumber components still exist in the gradient because some data originate from large scattering angle. For high-frequency inversion, the velocity models are generally not far from real ones; hence, in such cases, the low-wavenumber components in the gradient no longer play an important role in FWI, and may even reduce the convergence rate and inversion accuracy of FWI. To limit the low-wavenumber components in the gradient, Wang et al. (2016) separated the whole wavefield into the up-going wavefield and down-going wavefield based on F–K transform and only extracted the effective wavefield components to calculate the gradient; this method can significantly reduce the generation of low-wavenumber components, but the amount of computation and storage it requires is typically unacceptable. Xie (2015) implemented wavenumber filtering in the angle domain. He employed the scattering angle calculated by the Poynting vector to weigh the gradient and used the small scattering angle information to construct the short-wavelength component of the velocity model, thereby accelerating the convergence rate of the inversion. Subsequently, Jeong et al. (2018) adopted the optical flow method to calculate the scattering angle and found it to be more stable than the Poynting vector. However, both methods which include the Poynting vector and the optical flow method require a large amount of calculation.

In least-squares reverse time migration, Yang and Zhang (2018) proposed an angle-dependent factor weighted (essentially scattering angle weighted) gradient formula, which could effectively suppress low-wavenumber components and emphasize the gradient in the deep part without the need for the Poynting vector or optical flow method. Therefore, we introduce this method into FWI and derive the gradient formula of FWI based on scattering angle weighted. To better ensure the stability of FWI, we further propose a type of hybrid gradient, which combines the conventional gradient of FWI with the scattering angle weighted gradient in each inversion frequency band on the basis of the empirical formula of the hybrid weighting coefficient given in this study. With the proposed method, we can use more low-wavenumber components in some initial frequency bands to ensure the stability of inversion, and use more high-wavenumber gradient in some high-frequency inversion to improve the convergence rate and inversion accuracy.

2. Principle

2.1. Basic principle of FWI in the time domain

The objective function of FWI based on the L2 norm can be defined as (Tarantola, 1984)

$$E(\mathbf{v}) = \frac{1}{2}\sum_{(s,r)}[\mathbf{d}_{cal}(\mathbf{x}_r,\mathbf{x}_s) - \mathbf{d}_{obs}(\mathbf{x}_r,\mathbf{x}_s)]^T[\mathbf{d}_{cal}(\mathbf{x}_r,\mathbf{x}_s) - \mathbf{d}_{obs}(\mathbf{x}_r,\mathbf{x}_s)] \tag{1}$$

where $\mathbf{v}$ denotes the velocity model, $E(\mathbf{v})$ represents the objective function, $\mathbf{x}_r$ signifies the receiver position, $\mathbf{x}_s$ signifies the source position, $\mathbf{d}_{cal}$ denotes the simulated data, $\mathbf{d}_{obs}$ stands for the observed data, and the superscript T represents matrix transposition. Due to the ill-posed characteristics of the seismic inversion problem, the objective function shown in Eq. (1) is difficult to formulate directly, and iterative gradient algorithms are often used to restore the velocity model.

Herein, we use the adjoint state method (Plessix, 2006) to calculate the gradient and can obtain

$$g(\mathbf{x}) = -\sum_{(s,r)}\int \frac{2}{v(\mathbf{x})^3}\frac{\partial^2 U(\mathbf{x},t,\mathbf{x}_s)}{\partial t^2}\lambda(\mathbf{x},t,\mathbf{x}_r)\mathrm{d}t \tag{2}$$

where $\mathbf{x}$ represents the spatial position, $g(\mathbf{x})$ is the gradient, $v(\mathbf{x})$ denotes the velocity, $U(\mathbf{x},t,\mathbf{x}_s)$ is the forward-propagated wavefield perturbed by the source wavelet at point $\mathbf{x}_s$, which can be calculated by forward modeling, $\lambda(\mathbf{x},t,\mathbf{x}_r)$ is the back-propagated wavefield perturbed by the residual record at point $\mathbf{x}_r$, which can be calculated by reverse time extrapolation. Then we use the conjugate gradient algorithm based on gradient preconditioning and express the updating process of the velocity model as

$$\begin{cases} m_{k+1} = m_k + \alpha_k y_k \\ y_k = \begin{cases} -\mathbf{Q}g_k & k = 1 \\ -\mathbf{Q}g_k + \beta_k y_{k-1} & k \geq 2 \end{cases} \end{cases} \tag{3}$$

where k represents the number of iterations, β is the correction factor of the conjugate gradient, y is the conjugate gradient, α denotes the step length, and $\mathbf{Q}$ stands for the gradient preconditioning operator.

2.2. Strategy of multi-scale inversion

To prevent the objective function from falling into local minima, Bunks et al. (1995) proposed the idea of multi-scale in the time domain. They applied a filtering method to divide seismic data into different frequency components and scales, thus forming a serial inversion strategy from low frequency (large scale) to high frequency (small scale). The main process of the time-domain multi-scale FWI can be written as follows.

(1) Set the maximum frequency of the initial inversion model, as well as the maximum and minimum inversion velocities.
(2) Determine the grid step of the model according to the accuracy of the spatial difference, maximum frequency, and minimum velocity of the forward modeling. Then, provide the initial model of the frequency band.

(3) Filter the original source wavelet and seismic record to obtain the source wavelet and seismic record participating in the inversion of the frequency band.
(4) Perform time-domain FWI until the end of the frequency band inversion.
(5) Repeat Step (2) and the following steps to perform the inversion for the next frequency band. The initial model of the next frequency band is the inversion result of the previous frequency band obtained in Step (4) until the inversion of all frequency bands is completed.

The frequency band selection in Step (3) is the core issue in the time-domain multi-scale FWI. This study adopts the frequency band calculation formula proposed by Boonyasiriwat et al. (2009), which is given as

$$f_{N+1} = \frac{\sqrt{h^2 + z^2}}{z} f_N \tag{4}$$

where N denotes the serial number of the frequency band, f_N is the cut-off frequency of the Nth frequency band, f_{N+1} represents the cut-off frequency of the $(N+1)$th frequency band, h is half of the maximum offset, and z is the maximum depth.

3. Hybrid gradient formula for FWI based on scattering angle weighted

Eq. (2) indicates that the gradient of FWI is calculated from the cross-correlation between the forward-propagated wavefield of source wavelet and the back-propagated wavefield of residual record. Alkhalifah (2015) and Yao et al. (2020) indicated that the wavenumber components of the gradient are related to the frequency components of the data and the scattering angle between the shot and receiver points; a wavenumber component can be expressed as

$$\mathbf{K} = \frac{\omega}{v} \cos\left(\frac{\theta}{2}\right) \mathbf{n} \tag{5}$$

where $\mathbf{K}$ denotes the wavenumber, v is the velocity, ω denotes the angular frequency, $\mathbf{n}$ represents the unit vector of the wavenumber direction, and θ is the scattering angle.

As shown in Fig. 1, the vectors $\mathbf{n}_s$ and $\mathbf{n}_r$ denote the direction of the wave propagating from the source point to the scattering point and the scattering point to the receiver point, respectively. The scattering angle θ is the opening angle between $\mathbf{n}_s$ and $\mathbf{n}_r$.

It can be seen from Eq. (5) that the level of wavenumber is closely related to the size of the scattering angle. A large scattering angle generally corresponds to low wavenumber, while small scattering angle often corresponds to high wavenumber. Therefore, when FWI is implemented in some low-frequency bands, there will be plenty of low-wavenumber components which contribute to avoiding local minima of low-frequency inversion. And when FWI is implemented in some high-frequency bands, lots of low-wavenumber components are also abundant in the gradient because some data originate from large scattering angle. However, for high-frequency inversion, the velocity models are usually not far from real velocity model, so for such cases, the low-wavenumber components are no longer needed too many to ensure the stability of FWI, and they even will reduce the convergence rate and inversion accuracy of FWI.

Yang and Zhang (2018) proposed an angle-dependent factor weighted (essentially scattering angle weighted) gradient formula in the field of least-squares reverse time migration, which significantly reduced the low-wavenumber components in the gradient and improved the accuracy of deep inversion. In this paper, the idea is introduced into FWI, and the gradient formula of FWI based on scattering angle weighted is further derived.

3.1. Gradient formula for FWI based on scattering angle weighted

To reduce the low-wavenumber components in the gradient and compensate for the lack of deep illumination, the conventional gradient (Eq. (2)) of FWI is weighted:

$$g_w(\mathbf{x}) = -\sum_{(s,r)} \int \frac{2}{v(\mathbf{x})^3} \frac{\partial^2 U(\mathbf{x}, t, \mathbf{x}_s)}{\partial t^2} \lambda(\mathbf{x}, t, \mathbf{x}_r) w dt \tag{6}$$

where $g_w(\mathbf{x})$ is the weighted gradient at point $\mathbf{x}$, and w denotes the weighted term of the scattering angle, which is taken as $\cos^2(\theta/2)$. Fig. 2 shows the schematic description of the scattering angle weighting factor $\cos^2(\theta/2)$, and as the scattering angle increases from 0° to 180°, the weighting factor gradually changes from 1 to 0. Therefore, in theory, applying this weighting factor to the conventional gradient can effectively reduce the low-wavenumber components because low-wavenumber components usually appear on the wave propagation path with a large scattering angle (close to 180°). Moreover, for a fixed offset, the scattering angle of the deep part is normally smaller than that of the shallow part, so this weighting factor assigns a relatively large weight to the deep part of the gradient, which can greatly make up for the lack of deep illumination.

Obviously, we should determine the value of the scattering angle by using Eq. (6). One way is to use the Poynting vector or optical flow method to directly obtain the scattering angle θ (Xie,

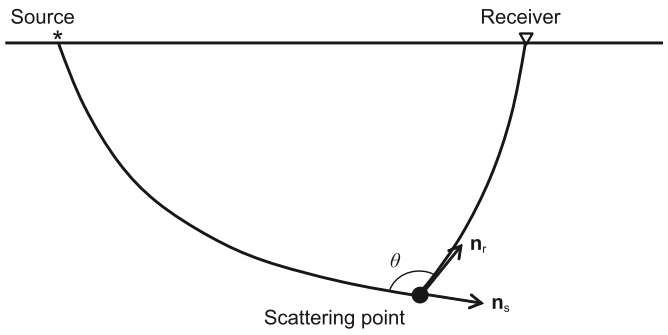

Fig. 1. Schematic description of scattering angle.

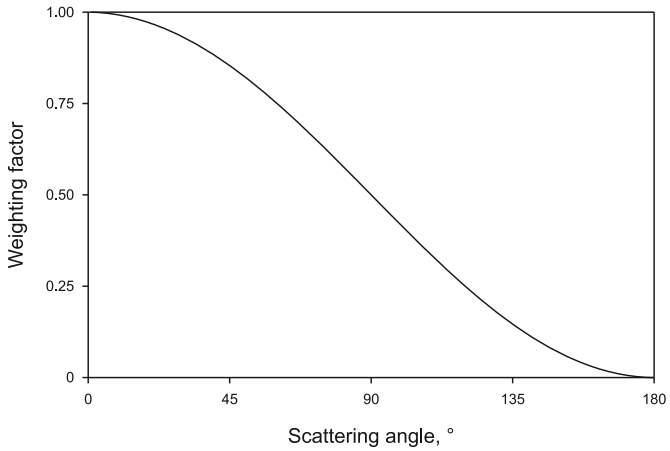

Fig. 2. Schematic description of the scattering angle weighting factor.

2015; Alkhalifah, 2015; Jeong et al., 2018); however, because the two methods need to calculate the scattering angle of each point and each moment in the velocity model in each iteration of FWI, the amount of computation required increases, thereby reducing the calculation efficiency of FWI. To avoid the direct calculation of the scattering angle, we use the following calculation formula and its derivation process is detailed in Appendix A.

$$g_{\mathrm{w}}(\mathbf{x}) = \frac{1}{2v(\mathbf{x})}\nabla^2\left(\sum_{(\mathrm{s,r})}\int U(\mathbf{x},t,\mathbf{x}_{\mathrm{s}})\lambda(\mathbf{x},t,\mathbf{x}_{\mathrm{r}})\mathrm{d}t\right) \tag{7}$$

Eq. (7) indicates that the weighted gradient $g_{\mathrm{w}}(\mathbf{x})$ calculated by Eq. (6) can be equivalent to the Laplace operation on the intermediate gradient $g_{\mathrm{i}}(\mathbf{x})$ and then multiplied with the coefficient $1/2v$, which skillfully avoids the direct calculation of the scattering angle θ.

3.2. Hybrid gradient method

Low-wavenumber components are necessary to ensure the stability of the inversion algorithms, especially for the low-frequency parts of multi-scale inversion in FWI. The gradient preconditioning method based on scattering angle weighted is not expected to be fully applied to low-frequency inversion, and it is only expected to be used partially in some high-frequency bands so as to reduce the low-wavenumber components of the gradient. Even so, due to the use of Laplace operation, this method still needs to be used carefully to prevent it from falling into local minima. Therefore, the applicability of this method is limited. To solve the problem, we further propose a new type of hybrid gradient for FWI, which can be described by the following equation:

$$g_{\mathrm{h}}(\mathbf{x}) = \varepsilon g_{\mathrm{w}}(\mathbf{x}) + (1-\varepsilon)g(\mathbf{x}) \tag{8}$$

where $g_{\mathrm{h}}(\mathbf{x})$ is the hybrid gradient at point $\mathbf{x}$, $g_{\mathrm{w}}(\mathbf{x})$ is the weighted gradient at point $\mathbf{x}$, $g(\mathbf{x})$ is the gradient at point $\mathbf{x}$, and ε is the hybrid weighting coefficient. The empirical formula for the hybrid weighting coefficient is directly given as

$$\varepsilon_N = 0.9\frac{f_N}{f_{\max}} + 0.1 \tag{9}$$

where ε_N is the hybrid weighting coefficient of the Nth frequency band and f_N denotes the cut-off frequency of the Nth frequency band calculated using Eq. (4). Meanwhile, $f_{\max}$ is the maximum effective frequency of the shot gather, which can be obtained using the spectrum analysis of the shot gather before inversion.

From Eq. (9), we can see that the hybrid weighting coefficient always remains unchanged in the same frequency band. Moreover, the hybrid weighting coefficient in the low-frequency band is much smaller than that in the high-frequency band. Hence, based on the hybrid gradient, more low-wavenumber components can be used in some initial frequency bands to ensure the stability of inversion, and more high-wavenumber components can be used in some high-frequency inversion to improve the convergence rate and inversion accuracy. Theoretically, the adaptability of HGFWI has been significantly enhanced.

4. Synthetic data experiment

The Marmousi velocity model is applied to the inversion test in this paper, which has 461 and 176 sampling points in the horizontal and vertical directions, respectively (as shown in Fig. 3), and the spatial sampling interval is 20 m. The smoothed velocity model is taken as the initial model (as shown in Fig. 4). The survey line

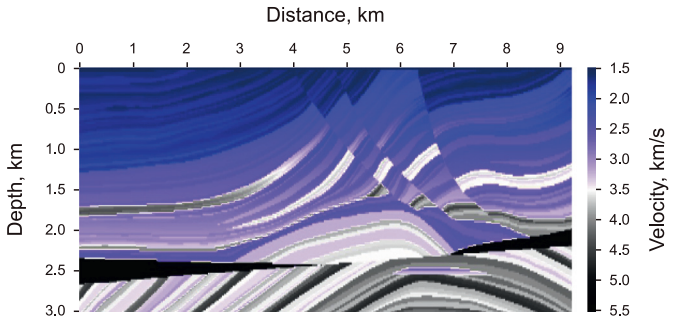

Fig. 3. Marmousi model.

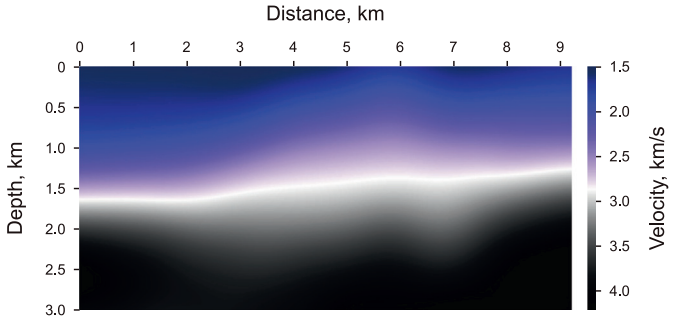

Fig. 4. Initial model.

contains 461 shots, which are evenly distributed on the surface with the interval of 20 m. Meanwhile, each shot has 461 geophones to receive. Besides, a Ricker wavelet with a 20 Hz dominant frequency is used to generate the data. The time sampling step is 0.5 ms and the maximum record time is 3.5 s. A hybrid absorbing boundary condition (Xie et al., 2020) is used for boundary processing.

Based on the aforementioned methods and experiment parameters, this paper conducts a multi-scale FWI experiment based on hybrid gradient. The experiment is divided into 5 inversion bands, and each band is iterated 20 times. Then, we determine the maximum effective frequency of the shot gather, and perform the spectrum analysis on the shot gather. The normalized amplitude spectrum obtained is shown in Fig. 5; $f_{\max}$ is set to 50. Therefore, the

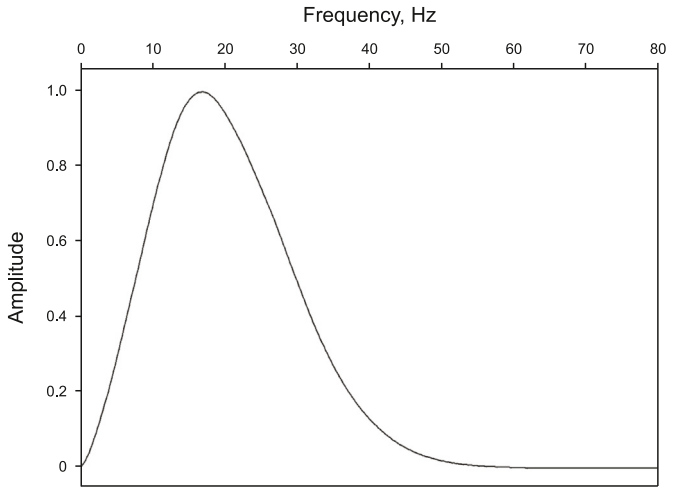

Fig. 5. Normalized amplitude spectrum of shot gather.

high cut-off frequencies for the 5 inversion bands are 5, 8.26, 13.64, 22.52, and 37 Hz, and the hybrid weighting coefficients of each frequency band are 0.19, 0.25, 0.35, 0.51, and 0.77, respectively.

Fig. 6(a)–(c) show the conventional gradient section, scattering angle weighted gradient section, and the hybrid gradient section after 1 iteration in the first frequency band, respectively. Fig. 7(a)–(c) present the wavenumber spectra corresponding to Fig. 6(a)–(c), respectively. From Fig. 6(a) (the point indicated by the red arrows), we can observe that the low-wavenumber components are particularly obvious in the conventional gradient section. Moreover, we observe that large energy at the center of the wavenumber spectra (Fig. 7(a)), indicating low-wavenumber components. As shown in Figs. 6(b) and 7(b), the low-wavenumber components are greatly reduced in the scattering angle weighted gradient section; this condition may lead to instability. In Figs. 6(c) and 7(c), the hybrid gradient just reduces very few low-wavenumber components, which will help maintain the stability of FWI in low-frequency bands.

Fig. 8 shows the gradient section after 1 iteration in the fourth

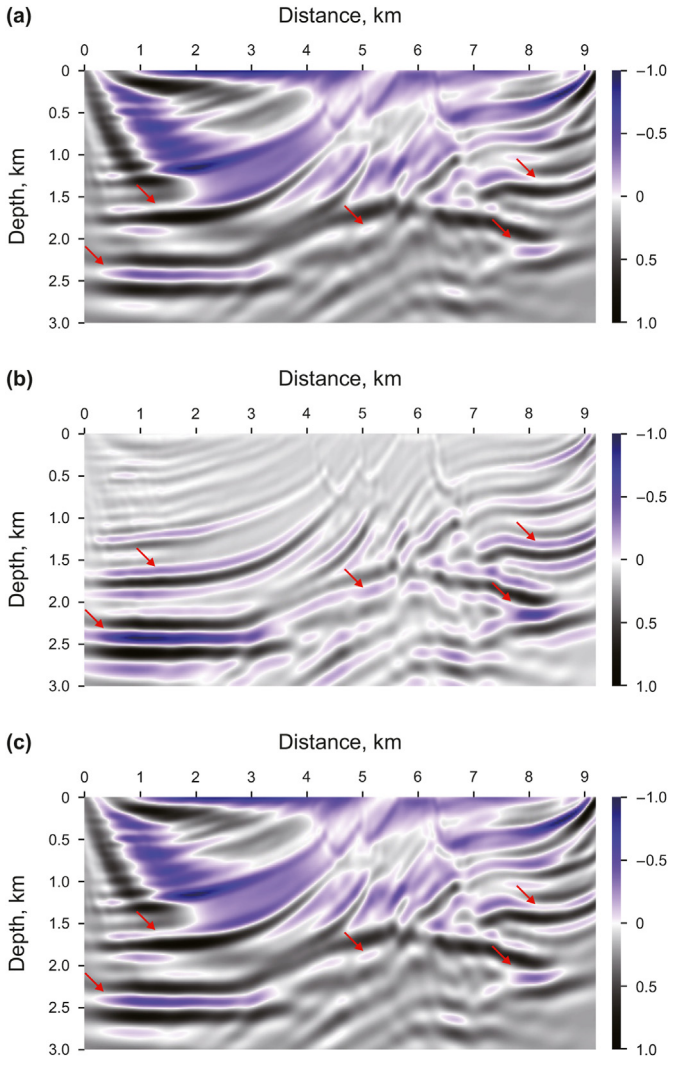

Fig. 6. Gradient section after 1 iteration in the first frequency band: (**a**) conventional gradient; (**b**) scattering angle weighted gradient; (**c**) hybrid gradient.

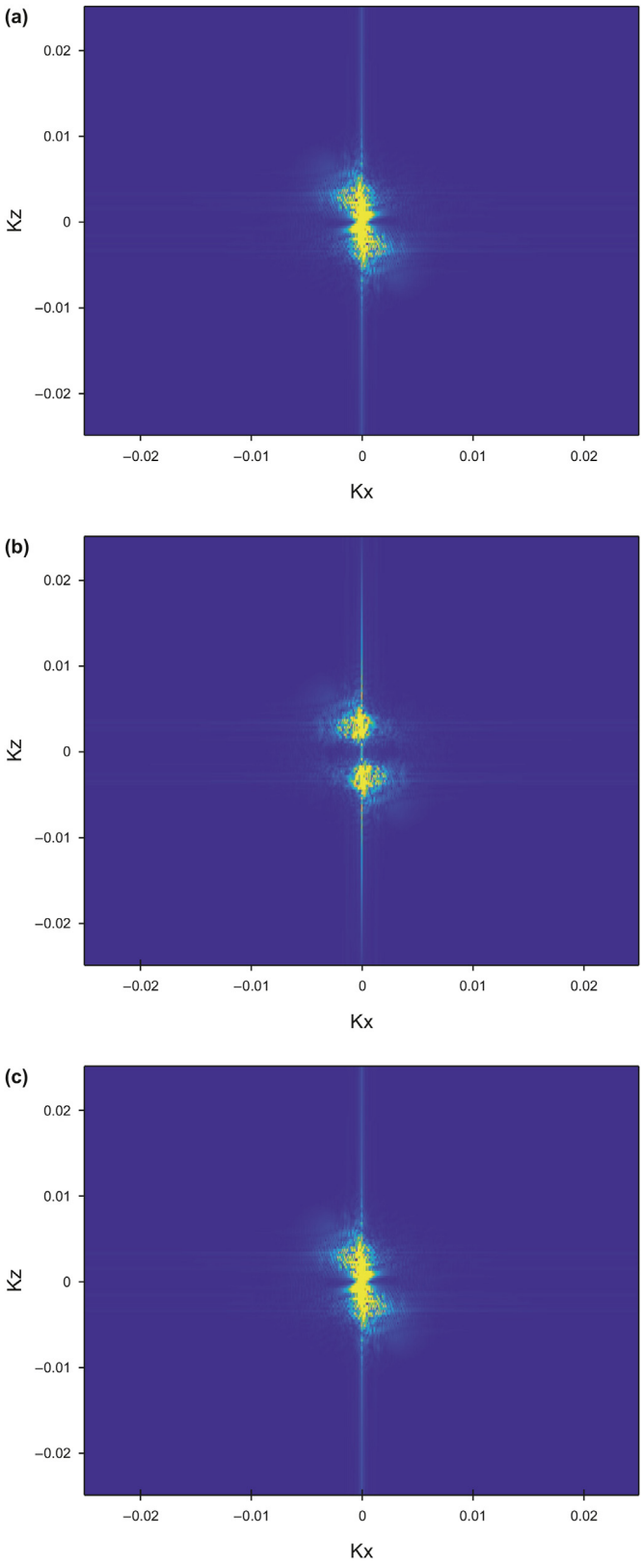

Fig. 7. Normalized wavenumber spectra corresponding to Fig. 6: (**a**) conventional gradient; (**b**) scattering angle weighted gradient; (**c**) hybrid gradient.

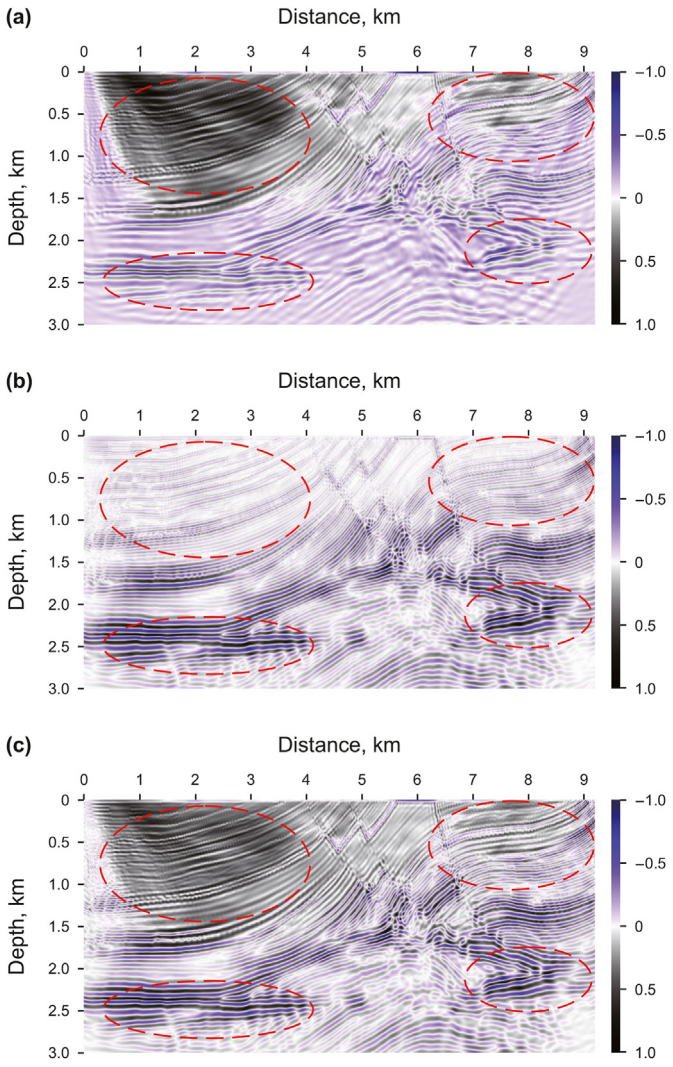

Fig. 8. Gradient section after 1 iteration in the fourth frequency band: (**a**) conventional gradient; (**b**) scattering angle weighted gradient; (**c**) hybrid gradient.

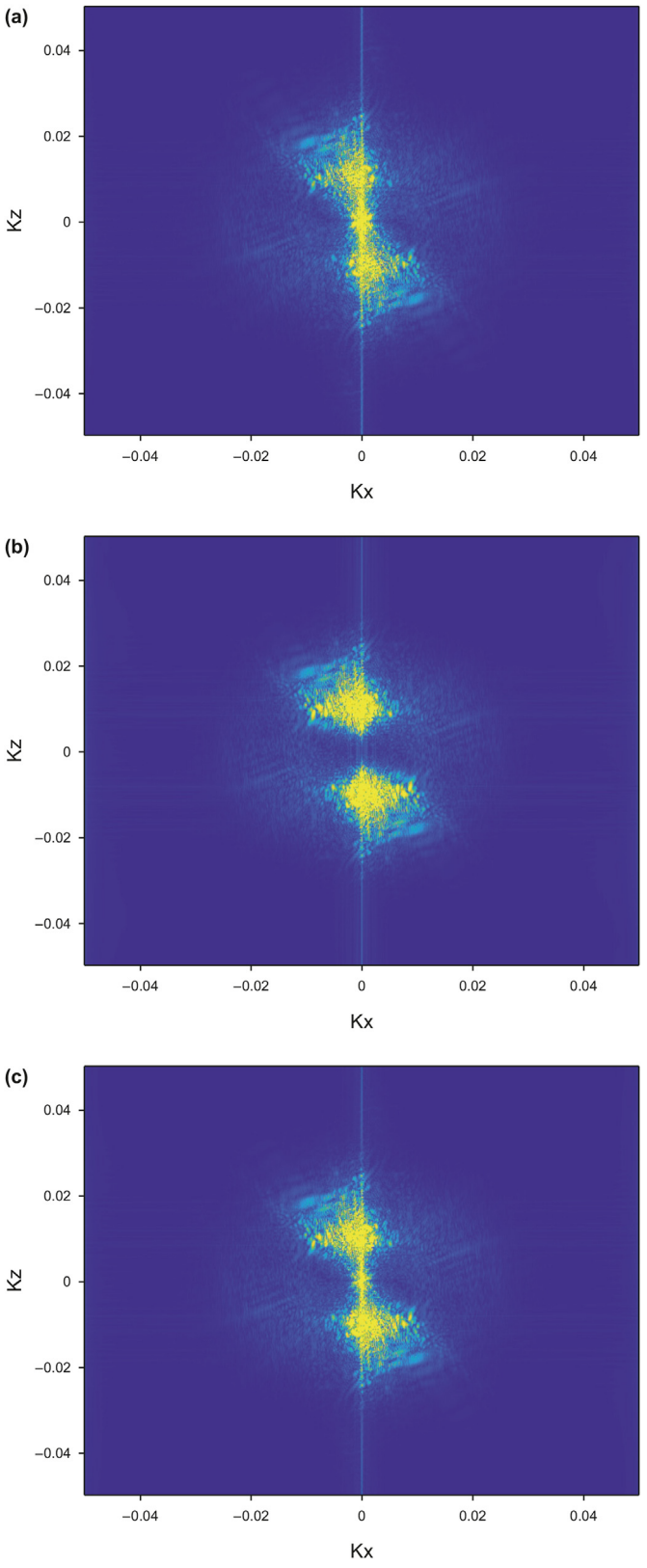

Fig. 9. Normalized wavenumber spectra corresponding to Fig. 8: (**a**) conventional gradient; (**b**) scattering angle weighted gradient; (**c**) hybrid gradient.

frequency band. Many low-wavenumber components can be observed in the shallow layer of the original gradient section in Figs. 8(a) and 9(a) (points indicated by the dashed red circles). These components mask the gradient energy of the deep part. In addition, the low-wavenumber components in the gradient are effectively suppressed using the scattering angle weighted from Figs. 8(b) and 9(b). As shown in Figs. 8(c) and 9(c), the low-wavenumber components are reduced in the hybrid gradient section; such condition accelerates the convergence rate of the inversion. Moreover, the energy of the shallow and deep areas is particularly balanced and can thus improve the inversion accuracy of the deep structure.

Fig. 10 illustrates the inversion result of conventional FWI after 20 iterations in the second frequency band. Fig. 11 shows the inversion result of the proposed method after 1 iteration in the second frequency band. Comparing Figs. 10 and 11, it can be seen that the inversion effect of FWI based on the hybrid gradient after 1 iteration in the second frequency band is better than that of the conventional FWI after 20 iterations in the second frequency band.

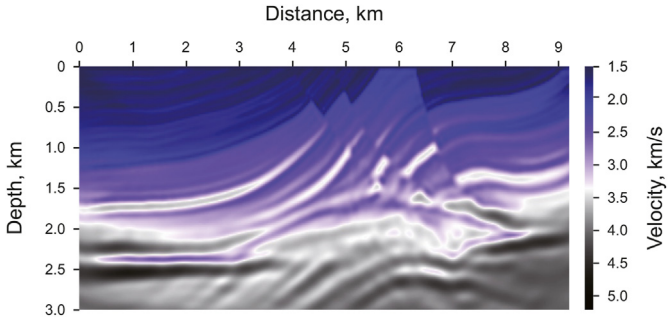

Fig. 10. The result of conventional FWI after 20 iterations in the second frequency band.

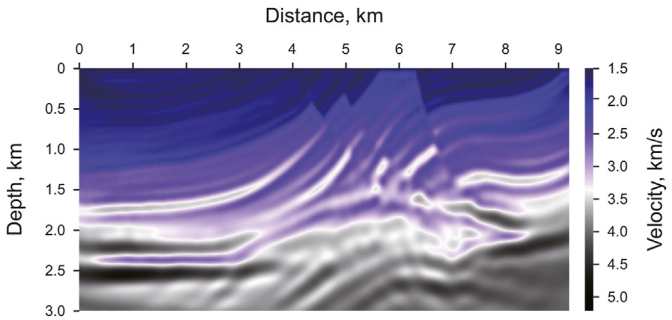

Fig. 11. The result of HGFWI after 1 iteration in the second frequency band.

To compare the inversion effects of the two methods more clearly, we extract the velocity curves at $x = 2540$ m and $x = 7800$ m from the sections in Figs. 10 and 11, respectively, and compare them with the real velocity curve. In Fig. 12, the green, blue, red, and black lines represent the initial velocity, the velocity of the conventional FWI, the velocity of the FWI based on the hybrid gradient, and the real velocity, respectively. The calculation time required for the two methods is shown in Table 1. It should be noted that the experimental environment used in this work is a GPU (Tesla K40) with 28 cards. As shown in Figs. 10–12, and Table 1, the proposed method can obtain a relatively high inversion accuracy with only half of the iterations of the conventional FWI in a short amount of time; hence, its convergence rate is high.

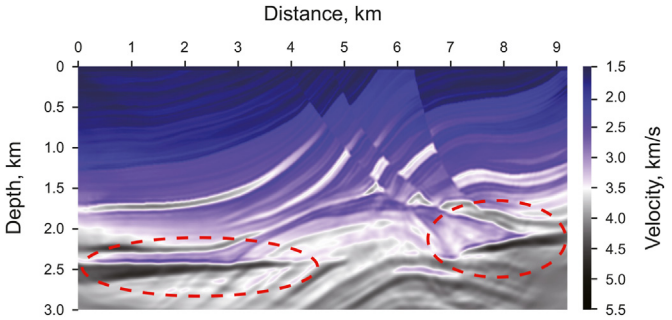

Fig. 13. The result of conventional FWI after 20 iterations in the fifth frequency band.

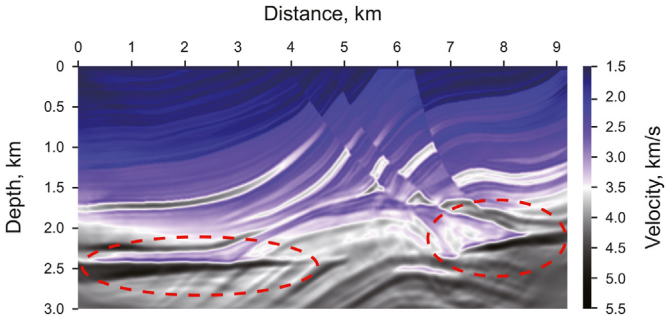

Fig. 14. The result of HGFWI after 20 iterations in the fifth frequency band.

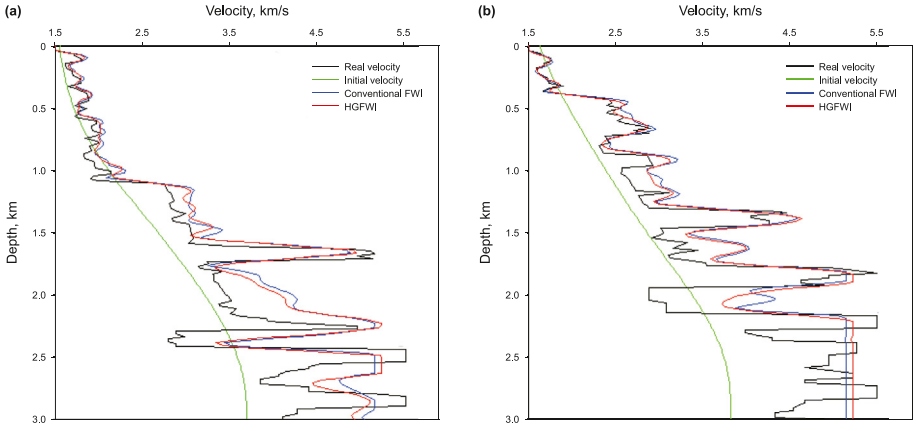

Fig. 12. Velocity curves: (**a**) $x = 2540$ m; (**b**) $x = 7800$ m.

Table 1
Calculation time comparison.

FWI method	Computing environment	Iterations	Average time per iteration, min	Total time, min
Conventional FWI	Tesla K40	40	3.58	143
HGFWI	Tesla K40	21	4.05	85

Table 2
Calculation time comparison.

FWI method	Computing environment	Iterations	Total time, min
Conventional FWI	Tesla K40	100	896
HGFWI	Tesla K40	100	1007

Table 3
E_{res} comparison.

FWI method	E_{res}
Conventional FWI	0.104%
HGFWI	0.028%

Figs. 13 and 14 illustrate the inversion results of the conventional FWI method and the proposed method, respectively, after 20 iterations in the fifth frequency band. Table 2 shows the calculation time required for the two inversions. From Figs. 13 and 14 (marked by the dashed red circle) and Table 2, we can observe that when the numbers of iterations are the same, the FWI based on the hybrid gradient achieves a much higher inversion accuracy than the conventional FWI, especially for the strata of deep high-velocity bodies. Moreover, the proposed method requires minimal calculation time. We extract the velocity curves at $x = 2540$ m and $x = 7800$ m from the sections in Figs. 13 and 14, respectively, and compare them with the real velocity curve. In Fig. 15, the green, blue, red, and black lines denote the initial velocity, the velocity of the conventional FWI, the velocity of the proposed method, and the real velocity, respectively. It can be seen from Fig. 15(a) and (b) that, compared with conventional FWI at 2540 m or 7800 m, the velocity curve of the proposed method is closer to the actual velocity curve. The results further verify that the proposed method achieves a relatively high inversion accuracy, especially for deep high-velocity bodies.

In order to quantify the inversion accuracy, the following calculation formula (Ben-Hadj-Ali et al., 2011) is used to quantitatively compare the final model residuals of the two methods, and the results are shown in Table 3.

$$E_{res} = \frac{\|m_{result} - m_{real}\|^2}{\|m_{real}\|^2} \times 100\% \tag{10}$$

where E_{res} represents the model residuals, m_{result} and m_{real} are the final inversion result and the real velocity model, respectively.

Normalized data residual and its partially enlarged view (enlarging the part with residual less than 0.2) are shown in Fig. 16(a) and (b), respectively. In Fig. 16, the blue, and red curves are the convergence curves of the conventional FWI and FWI based on the hybrid gradient, respectively. As observed from Fig. 16, the FWI based on the hybrid gradient has a faster convergence rate and smaller residual error. In summary, the proposed method achieves better inversion results than the conventional method.

5. Field marine seismic data inversion

We performed experiment on field marine seismic line to check the inversion adaptability of HGFWI. The survey line adopts the streamer acquisition method of shooting on the right and receiving on the left. The minimum offset is 100 m. There are 2699 shots in total, each shot has 240 hydrophones to receive. The intervals between shots and receivers are both 25 m. The depths of shots and receivers are both 12.5 m. The recording time is 7 s. The finite-difference accuracy of wavefield continuation is eighth order in space and second order in time. Meanwhile, the time sampling step is 1 ms.

Here the section ranging from 35 to 70 km of the whole survey line is intercepted as the inversion test area. The inversion process is divided into four inversion frequency bands (high cut-off frequencies are 5, 8, 15, 23 Hz, respectively), and 50 iterations are performed for each frequency band. Fig. 17(a) shows the initial model, which is constructed from migration velocity analysis. Fig. 17(b) shows the final FWI result.

Fig. 18 shows the results of reverse time migration, where Fig. 18(a) is the imaging result based on the initial model and Fig. 18(b) is the imaging result based on the model obtained from the HGFWI. It can be seen from Fig. 17(b) that the HGFWI can finely describe the high-resolution velocity model of the subsurface structure. And compared with Figs. 17(b) and 18(b), the imaging profile has good continuity of events, clear fault points and its structural feature is in excellent agreement with the velocity inversion result. Fig. 19(a) and (b) show the simulated seismic record and observed seismic record of the 1801th shot, respectively. Fig. 20 illustrates that the waveform comparison chart of the 1st trace of the 1801th shot. From Figs. 19 and 20, we can see that the simulated seismic record can match well with the observed seismic record. Fig. 21(a) and (b) display the common imaging gather with the initial model and the final FWI result, respectively. The position of the common imaging gather is 55.625 km. Compared with Fig. 21(a) and (b), we can see that the events in Fig. 21(b) are closer to the horizontal than in Fig. 21(a), which illustrates that the inversion result is closer to the real velocity model. In summary, our proposed method can be highly applicable to the FWI for field data.

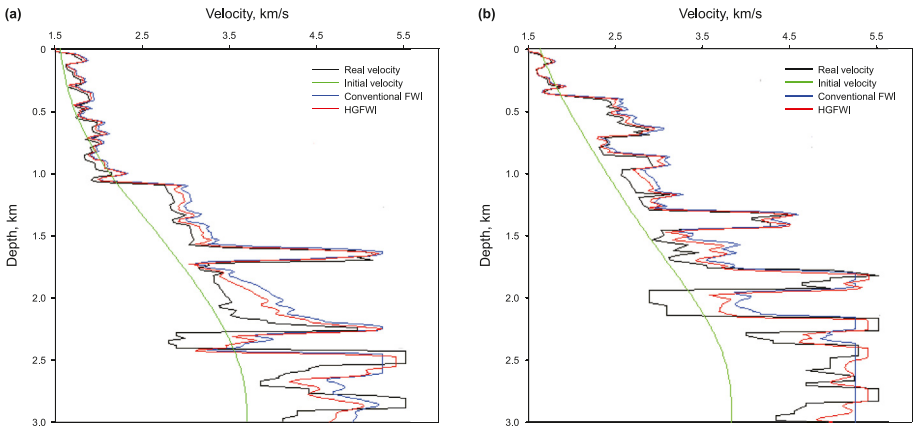

Fig. 15. Velocity curves: (**a**) $x = 2540$ m; (**b**) $x = 7800$ m.

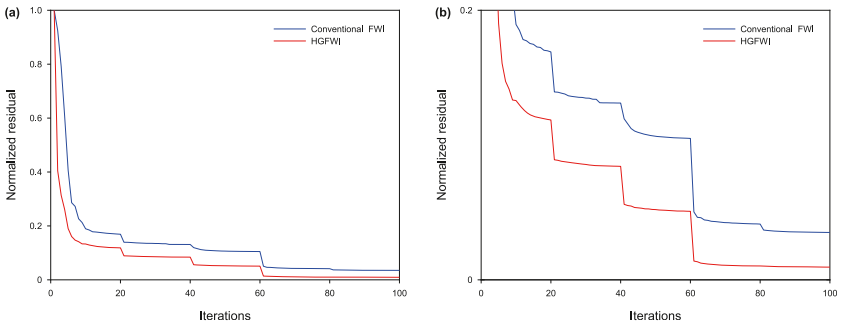

Fig. 16. Normalized data residual: (**a**) global convergence diagram; (**b**) partially enlarged view.

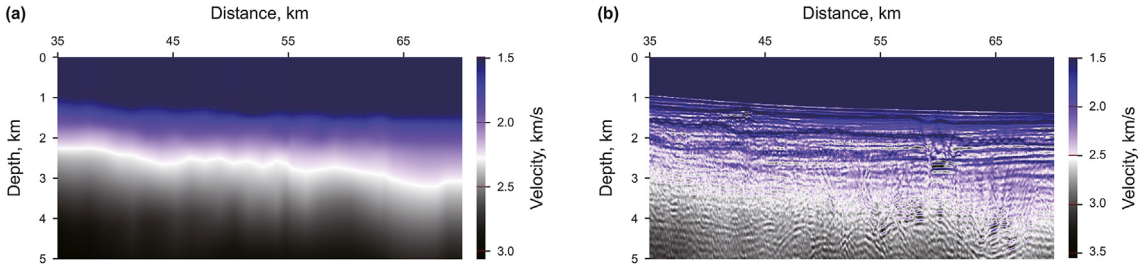

Fig. 17. Velocity model: (**a**) initial model; (**b**) the result of HGFWI.

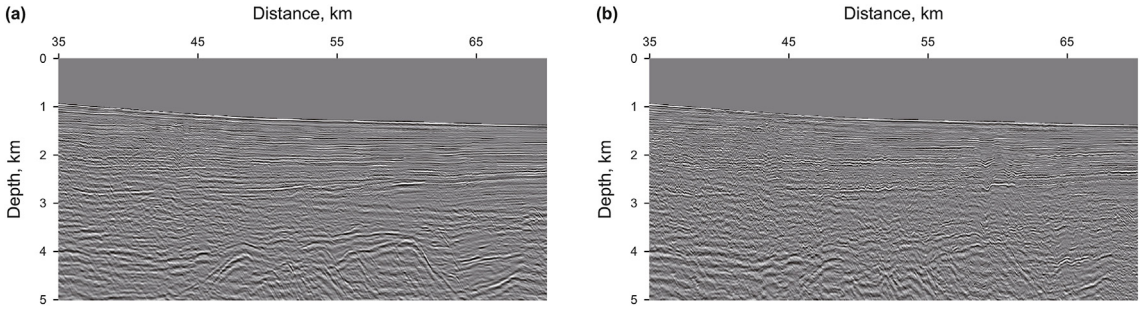

Fig. 18. The results of reverse time migration: (**a**) the imaging result based on the initial model; (**b**) the imaging result based on the model obtained from the HGFWI.

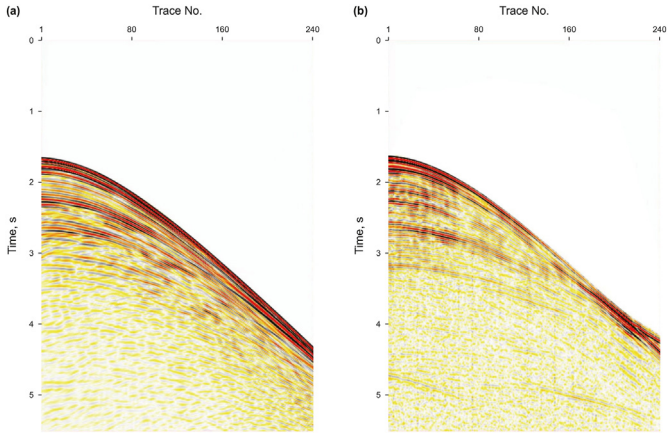

Fig. 19. Seismic record: (**a**) simulated data; (**b**) observed data.

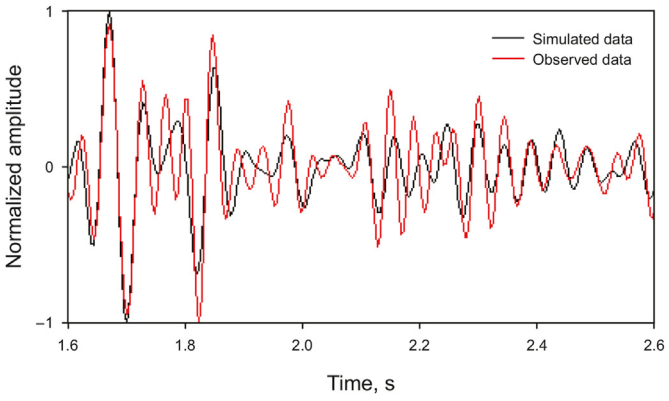

Fig. 20. The waveform comparison chart of the 1st trace of the 1801th shot.

6. Conclusions and prospect

This paper proposes a hybrid gradient, which combines the conventional gradient of FWI with the scattering angle weighted gradient based on an empirical formula given in the study. The experimental results of the Marmousi model reveal the following: the proposed method can preserve enough low-wavenumber components in the gradient in low-frequency inversion and

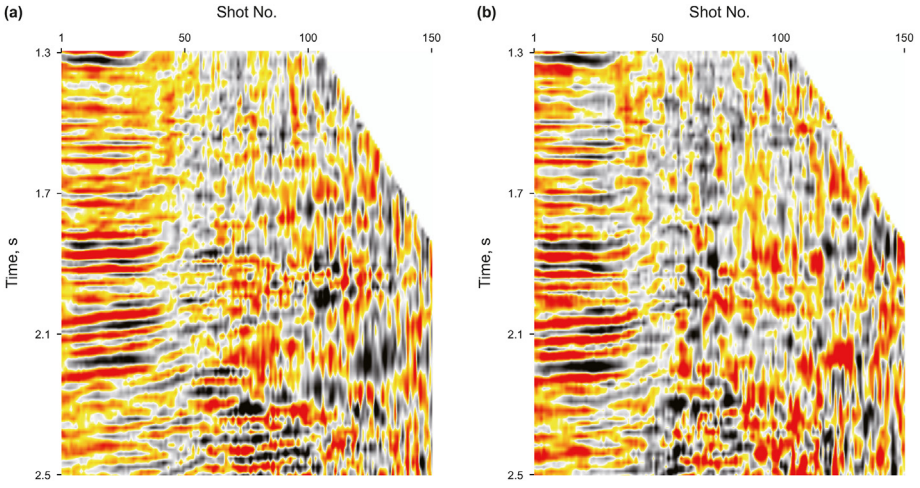

Fig. 21. Common imaging gather: (**a**) the initial model; (**b**) the final FWI result.

reduce lots of low-wavenumber components in high-frequency inversion, which leads to a stable and high accuracy FWI with high convergence rate, also it has a higher inversion accuracy for deep structures. And the result of marine seismic data shows that our proposed method can adapt to FWI for field data well, and obtain a high-precision velocity model of the subsurface structure.

This paper only implements two-dimensional multi-scale HGFWI. Subsequent research will focus on further extending the algorithm to three-dimensional inversion.

CRediT authorship contribution statement

Chuang Xie: Writing – original draft. **Zhi-Liang Qin:** Writing – review & editing. **Jian-Hua Wang:** Data curation. **Peng Song:** Methodology. **Heng-Guang Shen:** Investigation. **Sheng-Qi Yu:** Investigation. **Ben-Jun Ma:** Investigation. **Xue-Qin Liu:** Investigation.

Acknowledgements

This research was jointly supported by Young Scientists Cultivation Fund Project of Harbin Engineering University (79000013/003), the Mount Taishan Industrial Leading Talent Project, the Great and Special Project under Grant KJGG-2022-0104 of CNOOC Limited and the National Natural Science Foundation of China (42006064, 42106070, 42074138).

Appendix A

We calculate the intermediate gradient first, which shares a similar form to the imaging condition (Baysal et al., 1983) used in the conventional reverse time migration; that is,

$$g_{\mathrm{i}}(\mathbf{x}) = \sum_{(\mathrm{s},\mathrm{r})} \int U(\mathbf{x}, t, \mathbf{x}_{\mathrm{s}}) \lambda(\mathbf{x}, t, \mathbf{x}_{\mathrm{r}}) \mathrm{d}t \tag{A-1}$$

where $g_{\mathrm{i}}(\mathbf{x})$ is the intermediate gradient. Using Laplace transform on both sides of Eq. (A-1), we can obtain (Douma et al., 2010)

$$\nabla^2 g_{\mathrm{i}}(\mathbf{x}) = -2\left(\sum_{(\mathrm{s},\mathrm{r})} \int \frac{1}{v(\mathbf{x})^2} \frac{\partial U(\mathbf{x}, t, \mathbf{x}_{\mathrm{s}})}{\partial t} \frac{\partial \lambda(\mathbf{x}, t, \mathbf{x}_{\mathrm{r}})}{\partial t} dt - \sum_{(\mathrm{s},\mathrm{r})} \int \nabla U(\mathbf{x}, t, \mathbf{x}_{\mathrm{s}}) \cdot \nabla \lambda(\mathbf{x}, t, \mathbf{x}_{\mathrm{r}}) \mathrm{d}t\right) \tag{A-2}$$

where ∇^2 stands for the Laplacian operator and ∇ denotes the gradient operator. As the dot product of the spatial gradient vectors of forward- and back-propagated wavefields contains information of the scattering angle, we can perform the following transformation (Yang and Zhang, 2018):

$$\nabla P(\mathbf{x}, t, \mathbf{x}_{\mathrm{s}}) \cdot \nabla \lambda(\mathbf{x}, t, \mathbf{x}_{\mathrm{r}}) = -\sum_{(\mathrm{s},\mathrm{r})} \int \frac{1}{v(\mathbf{x})^2} \frac{\partial U(\mathbf{x}, t, \mathbf{x}_{\mathrm{s}})}{\partial t} \frac{\partial \lambda(\mathbf{x}, t, \mathbf{x}_{\mathrm{r}})}{\partial t} \cos\theta \mathrm{d}t \tag{A-3}$$

Substituting Eq. (A-3) into Eq. (A-2), we can obtain

$$\nabla^2 g_{\mathrm{i}}(\mathbf{x}) = -2\left(\sum_{(\mathrm{s},\mathrm{r})} \int \frac{1}{v(\mathbf{x})^2} \frac{\partial U(\mathbf{x}, t, \mathbf{x}_{\mathrm{s}})}{\partial t} \frac{\partial \lambda(\mathbf{x}, t, \mathbf{x}_{\mathrm{r}})}{\partial t} (1 + \cos(\theta)) \mathrm{d}t\right) \tag{A-4}$$

Substituting Eq. (A-4) into Eq. (6) leads to

$$g_{\mathrm{w}}(\mathbf{x}) = \frac{1}{2v(\mathbf{x})} \nabla^2 g_{\mathrm{i}}(\mathbf{x}) = \frac{1}{2v(\mathbf{x})} \nabla^2 \left(\sum_{(\mathrm{s},\mathrm{r})} \int U(\mathbf{x}, t, \mathbf{x}_{\mathrm{s}}) \lambda(\mathbf{x}, t, \mathbf{x}_{\mathrm{r}}) \mathrm{d}t\right) \tag{A-5}$$

where $g_{\mathrm{w}}(\mathbf{x})$ is the weighted gradient. Eq. (A-5) is consistent with Eq. (7) in the paper.

References

Alkhalifah, T., 2015. Scattering-angle based filtering of the waveform inversion gradients. Geophys. J. Int. 200 (1), 363–373. https://doi.org/10.1093/gji/ggu379.

Alkhalifah, T., Wu, Z.D., 2016. Multiscattering inversion for low-model wavenumbers. Geophysics 81 (6), R417–R428. https://doi.org/10.1190/GEO2015-0650.1.

Baysal, E., Kosloff, D., Sherwood, J., 1983. Reverse time migration. Geophysics 48 (11), 1514–1524. https://doi.org/10.1190/1.1441434.

Ben-Hadj-Ali, H., Operto, S., Virieux, J., 2011. An efficient frequency-domain full waveform inversion method using simultaneous encoded sources. Geophysics 76 (4), R109–R124. https://doi.org/10.1190/1.3581357.

Boonyasiriwat, C., Valasek, P., Routh, P., et al., 2009. An efficient multiscale method for time-domain waveform tomography. Geophysics 74 (6), WCC59–WCC68. https://doi.org/10.1190/1.3151869.

Bunks, C., Saleck, F.M., Zaleski, S., et al., 1995. Multiscale seismic waveform inversion. Geophysics 60 (5), 1457–1473. https://doi.org/10.1190/1.1443880.

Chen, G.X., Wu, R.S., Chen, S.C., 2018. Reflection multi-scale envelope inversion. Geophys. Prospect. 66 (7), 1258–1271. https://doi.org/10.1111/1365-2478.12624.

Douma, H., Yingst, D., Vasconcelos, I., et al., 2010. On the connection between artifact filtering in reverse-time migration and adjoint tomography. Geophysics 75 (6), S219–S223. https://doi.org/10.1190/1.3505124.

Fu, L., Feng, Z.C., Schuster, G.T., 2020. Multiscale phase inversion for 3D ocean-bottom cable data. Geophys. Prospect. 68 (3), 786–801. https://doi.org/10.1111/1365-2478.12878.

Huang, J.P., Cui, C., Liu, M.L., 2018. A hybrid multi-scale full waveform inversion method based on frequency-wavenumber filter and its implementation strategies. J. China U. Petrol. 42 (2), 50–59. https://doi.org/10.3969/j.issn.1673-5005.2018.02.006.

Jakobsen, M., Wu, R.S., 2018. Accelerating the T-matrix approach to seismic full waveform inversion by domain decomposition. Geophys. Prospect. 66 (6), 1039–1059. https://doi.org/10.1111/1365-2478.12619.

Jeong, W., Tsingas, C., Kim, Y.S., 2018. Full waveform inversion with angle-dependent gradient preconditioning using wavefield decomposition. J. Appl. Geophys. 159, 23–32. https://doi.org/10.1016/j.jappgeo.2018.07.016.

Ke, X., Shi, Y., Fu, X.F., et al., 2023. The *n*th power Fourier spectrum analysis for the generalized seismic wavelets. IEEE Trans. Geosci. Rem. Sens. 61, 5904010. https://doi.org/10.1109/TGRS.2023.3243184.

Li, X., Yao, G., Niu, F.L., et al., 2022. Waveform inversion of seismic first arrival acquired on irregular surface. Geophysics 87 (3), R291–R304. https://doi.org/10.1190/geo2021-0097.1.

Li, Y.Y., Alkhalifah, T., 2021. Extended full waveform inversion with matching filter. Geophys. Prospect. 69 (7), 1441–1454. https://doi.org/10.1111/1365-2478.13121.

Lian, S.J., Yuan, S.Y., Wang, G.C., et al., 2018. Enhancing low-wavenumber components of full-waveform inversion using an improved wavefield decomposition method in the time-space domain. J. Appl. Geophys. 157, 10–22. https://doi.org/10.1016/j.jappgeo.2018.06.013.

Plessix, R., 2006. A review of the adjoint-state method for computing the gradient of a functional with geophysical applications. Geophys. J. Int. 167 (2), 495–503. https://doi.org/10.1111/j.1365-246X.2006.02978.x.

Ren, Z.M., Dai, X., Bao, Q.Z., 2023. Finite-frequency sensitivity kernels and hierarchical traveltime and waveform inversion of direct and reflected waves from vertical seismic profile data. Geophysics 88 (4), R439–R452. https://doi.org/10.1190/geo2022-0358.1.

Ren, Z.M., Li, Z.C., Gu, B.L., 2019. Elastic reflection waveform inversion based on the decomposition of sensitivity kernels. Geophysics 84 (2), R235–R250. https://doi.org/10.1190/geo2018-0220.1.

Shipp, R.M., Singh, S.C., 2002. Two dimensional full wavefield inversion of wide-aperture marine seismic streamer data. Geophys. J. Int. 151 (2), 325–344. https://doi.org/10.1046/j.1365-246X.2002.01645.x.

Song, P., Tan, J., Liu, Z.L., et al., 2019. Time-domain full waveform inversion using the gradient preconditioning based on transmitted wave energy. J. Ocean Univ. China 18, 859–867. https://doi.org/10.1190/IGC2017-063.

Tang, Y.X., Lee, S., Baumstein, A., et al., 2013. Tomographically enhanced full wavefield inversion. In: 83rd Annual International Meeting. SEG, Expanded Abstracts, pp. 1037–1041. https://doi.org/10.1190/segam2013-1145.1.

Tarantola, A., 1984. Inversion of seismic reflection data in the acoustic approximation. Geophysics 49 (8), 1259–1266. https://doi.org/10.1190/1.1441754.

Wang, F., Donno, D., Chauris, H., et al., 2016. Waveform inversion based on wavefield decomposition. Geophysics 81 (6), R457–R470. https://doi.org/10.1190/geo2015-0340.1.

Xie, C., Song, P., Tan, J., et al., 2020. Cosine-type weighted hybrid absorbing boundary based on the second-order Higdon boundary condition and its GPU implementation. J. Geophys. Eng. 17 (2), 231–248. https://doi.org/10.1093/jge/gxz102.

Xie, X.B., 2015. An angle-domain wavenumber filter for multi-scale full waveform inversion. In: 85th Annual International Meeting. SEG, Expanded Abstracts, pp. 1132–1136. https://doi.org/10.1190/segam2015-5877023.1.

Yang, J.D., Zhu, H.J., Li, X.Y., et al., 2020. Estimating *P* wave velocity and attenuation structures using full waveform inversion based on a time domain complex-valued viscoacoustic wave equation: the method. J. Geophys. Res. Solid Earth 125 (6), e2019JB019129. https://doi.org/10.1029/2019JB019129.

Yang, K., Zhang, J.F., 2018. Least-squares reverse time migration with an angle-dependent weighting factor. Geophysics 83 (3), S299–S310. https://doi.org/10.1190/geo2017-0207.1.

Yao, G., da Silva, N.V., Kazei, V., et al., 2019a. Extraction of the tomography mode with nonstationary smoothing for full-waveform inversion. Geophysics 84 (4), R527–R537. https://doi.org/10.1190/geo2018-0586.1.

Yao, G., da Silva, N.V., Warner, M., et al., 2018. Separation of migration and tomography modes of full-waveform inversion in the plane wave domain. J. Geophys. Res. Solid Earth 123, 1486–1501. https://doi.org/10.3997/2214-4609.201800689.

Yao, G., da Silva, N.V., Warner, M., et al., 2019b. Tackling cycle skipping in full-waveform inversion with intermediate data. Geophysics 84 (3), R411–R427. https://doi.org/10.1190/geo2018-0096.1.

Yao, G., Wu, D., Wang, S.X., 2020. A review on reflection-waveform inversion. Petrol. Sci. 17 (1), 334–351. https://doi.org/10.1007/s12182-020-00431-3.